Q. J. R. Meteorol. Soc. (2003), **129**, pp. 777–797 doi: 10.1256/qj.02.45

Gravity waves over the eastern Alps: A synopsis of the 25 October 1999 event (IOP 10) combining *in situ* and remote-sensing measurements with a high-resolution simulation

By HANS VOLKERT[1]*, CHRISTIAN KEIL[1,3], CHRISTOPH KIEMLE[1], GORAZD POBERAJ[1,4], JEAN-PIERRE CHABOUREAU[2] and EVELYNE RICHARD[2]

[1]*Institut für Physik der Atmosphäre, DLR, Oberpfaffenhofen, Germany*
[2]*Université d'Aérologie, CNRS and Université Paul Sabatier, Toulouse, France*
[3]*ECMWF, Reading, UK*
[4]*Primorska Institute for Natural Sciences and Technology, Koper, Slovenia*

(Received 31 January 2002; revised 5 July 2002)

SUMMARY

In situ and lidar data acquired during six repetitive flight legs across Grossglockner (3797 m, highest summit of the eastern Alps) reveal a coherent structure of the mountain-wave field generated by a south-westerly cross-Alpine flow on 25 October 1999 during Intensive Observing Period (IOP) 10 of the Mesoscale Alpine Programme (MAP). The downward-looking laser system sampling at 100 Hz provides distinct wave-induced signatures in the layered clouds below the cruising altitude of about 11 km. Data obtained from three sondes dropped from the aircraft hint at mid-tropospheric wave breaking in the lee of the main Alpine crest. The measurements are juxtaposed with results from a nested, non-hydrostatic simulation (2 km horizontal resolution for the finest grid). Wave-cloud signatures in satellite images (from Meteosat and the National Oceanic and Atmospheric Administration satellites) are used for comparisons with the simulation in a region away from the aircraft track. Sensitivity experiments reveal the regular wave response to be induced by the background profile and re-enforced by the suitably spaced terrain.

KEYWORDS: Airborne lidar Föhn Mesoscale Alpine Programme Mountain waves

1. INTRODUCTION

Vertical disturbances within a predominantly horizontal flow of stably stratified air instigate wave motions, for which the Earth's gravity acts as the restoring force. These are termed *gravity waves*. *Mountain waves* constitute the important subset of gravity waves being generated by airflow across mountain ridges (Durran 1990). Since their discovery on the northern slopes of the Riesengebirge (border between Silesia and Bohemia, today Poland and the Czech Republic; cf. Whelan (2000), pp. 1–10) by glider pilots more than 60 years ago, mountain waves have been an incessant topic of atmospheric physics.

When flow and stability conditions are favourable the waves are generated in the vicinity of the ridges. They can be trapped below a certain level, and then they either propagate in a horizontal duct away from the mountain, or stationary waves develop for a time. The wave crests of the latter are often marked by stationary altocumulus lenticularis clouds. Alternatively, the waves propagate mainly vertically and steepen due to the decreasing air density to such an extent that overturning and mixing can suppress the wave motions. This process is termed *gravity-wave breaking* in analogy to breaking water waves at ocean shores.

During the Special Observing Period (SOP) of the Mesoscale Alpine Programme (MAP) 11 gravity-wave situations were investigated in project P6 (Bougeault *et al.* 2001), but wave breaking could not be directly sampled. This study concentrates on the appearance of mountain waves over different regions of the eastern Alps (i.e. to the east of the Brenner pass) in a south-westerly airflow during the period 0700–1500 UTC on 25 October 1999, which is part of Intensive Observing Period (IOP) 10. Characteristics of

* Corresponding author: Deutsches Zentrum für Luft- und Raumfahrt (DLR), Institut für Physik der Atmosphäre, Oberpfaffenhofen, D-82230 Wessling, Germany. e-mail: Hans.Volkert@dlr.de

the waves are revealed by combining *in situ*, remotely sensed lidar and dropsonde data from the research aircraft Falcon and satellite images, with a nested high-resolution numerical simulation.

The overall aim of this case-study is to precisely document the mountain-wave systems over the eastern Alps on 25 October 1999, to consistently check the findings with the help of a high-resolution simulation and, thus, to provide a sound starting point for systematic modelling studies. The addressed specific topics include indications of wave breaking in the dropsonde data, the extent to which observed wave-modulated cloud decks can be simulated, the interplay of wave trapping and continuous orographic forcing through adjacent massifs, and the existence of a 'cloud waterfall' in the lee of the Hohe Tauern range of the eastern Alps. The paper is organized as follows: relevant previous studies are summarized in the next section in order to elucidate the scope and novelty of this study. Background information on measuring and simulation systems is provided in section 3. Section 4 presents the general weather situation and all the measurements, while the simulation results and comparisons with the measurements are collected in section 5. The final section contains concluding remarks and an outlook.

2. Previous studies

Early, not commonly known, mountain-wave campaigns and later studies, which combined observation and simulation, are recapitulated to put this work into perspective.

In a seminal paper Küttner (1939) documents gravity-wave structures associated with föhn-type flows across various mountain ranges. Some 35 photographs of wave clouds, surface-pressure charts, ballon soundings and barogrammes from selected glider flights provide the background material. Such in-flight registrations of no less than 22 sailplanes, taking part in a contest on 21 May 1937, are used to map out three subsequent zones of wave-induced updraughts and downdraughts at right angles to the large-scale flow across the Riesengebirge (peak height 1603 m; Küttner 1939, his Fig. 32). Average horizontal wavelengths amount to 7 or 8 km with a variation between 4 and 10 km. Vertical velocities typically lie in the range 4 to 6 m s^{-1}, while the height difference along a streamline of 200 m to 500 m reveals a comparatively shallow wave amplitude. The flight of 14 September 1937 up to 6.8 km (Whelan 2000, p. 9) documented that wave-induced updraughts can cover the best part of the troposphere and that the wave clouds (local name: *moazagotl*) can extend from altocumulus to cirrus level.

Three years later a föhn-induced large wave over the eastern Alpine region carried a sailplane from 6.5 km up to the tropopause at 11.5 km on 11 October 1940. The situation was characterized by a southerly flow of about 17 m s^{-1}, ascent of 5 m s^{-1} in the lee of the Hohe Tauern, low-level wave clouds separated by 10 to 15 km, 40 km wavelengths documented by the accompanying motorized aircraft at medium level, and upper-level clouds extending well into the cirrus layer (see Krug-Pielsticker (1942) for a detailed description of this event and the mission).

During the years 1956 to 1959 mountain lee waves were systematically measured over the French Alps and their western foothills. Gerbier and Berenger (1961) present time–height diagrams up to 9 km of the sailplane flights with vertical velocities varying between $+6$ and -5 m s^{-1}, and balloon tracks exhibiting horizontal wavelengths of about 10 km. Their conclusions list as factors which determine size, strength and vertical extent of mountain waves, details of the relief, the inflow and stability profiles and complex interrelations between these, particularly in transient situations. Besides aircraft and balloon data Cruette (1976) systematically analyses three years of satellite imagery over Europe and retains over 80 cases of lee-wave-generated cloud-street systems (average wavelength 15 km; extension of system between 50 and 700 km).

More recently, Ralph *et al.* (1997) analyse remote-sensing data (lidar, wind profilers, satellite imagery) to investigate trapped waves within the Boulder area in the lee of the Rocky Mountains. They find an average wavelength of 15.8 ± 4.5 km from a sample of 24 cases together with temporal changes of up to 30% h^{-1} and conclude that the stationarity of wave systems has to be determined rather than assumed. Simulations of vertical-motion cells (maximum updraught 1.8 m s^{-1}) are made in a two-dimensional non-hydrostatic framework over an idealized obstacle and initialized with profiler and radiosonde data. Dean-Day *et al.* (1998) use aircraft data at 9 km altitude above this area to determine wave parameters for two events by inserting averaged observations into a wave equation from linear theory. The dominant waves are determined to range from 10 to 30 km. Chan *et al.* (1993) applied similar instruments at 20 km altitude above the southern tip of Greenland to observe a single major wave with a 60 km wavelength. This wave is also found in a realistic three-dimensional episode simulation with a nested non-hydrostatic model provided that the horizontal resolution is better than 4 km and the parametrized surface friction not too small (Leutbecher and Volkert 2000).

Mountain waves in Europe were extensively investigated above the Lake District hills (maximum elevation 891 m) in northern England. Shutts and Broad (1993) combined aircraft data at four altitudes up to about 7.5 km with measurements from multiple sonde releases with varying ascent rates, satellite imagery, and a limited-area non-hydrostatic dry simulation on a 2 km grid extending over 180 km $\times$ 180 km forced by a single upstream sounding. The dominant wavelength was found to be about 20 km with its maximum amplitude at an altitude of 3 km and vertical velocities up to 3.5 m s^{-1}. Control simulations including moisture proved that the wave response was not sensitive to humidity. Indications of wave-induced clouds were found in the simulation with a too strong diffusion of high humidity values downwind of the main hills. Elkhalfi *et al.* (1995) simulate the multi-aircraft traverse during IOP 3 of the Pyrenees Experiment (PYREX) in a hydrostatic two-dimensional framework and demonstrate that these approximations suffice for realistic estimates of the momentum-flux profile. Georgelin and Lott (2001) re-analyse the aircraft data (10 levels) of this case, carry out two-dimensional simulations (grid distance 0.7 km) and recover trapped waves with a dominant mode of 10 km wavelength and significant updraughts of about 5 m s^{-1}.

For the central Alpine region no comprehensive gravity-wave study is available from the pre-MAP SOP era (except the detailed conference contribution by Reinhardt (1963)). Long trains (up to 20 cycles) of short waves (300 to 600 m in length) in an outstanding snapshot of space imagery have more aesthetic value as the scarcity of relevant atmospheric background data inhibits thorough theoretical calculations (Volkert 1985). During the Alpine Experiment (ALPEX) special observing period in spring 1982 no strong föhn case occurred. On 8 November 1982 the Falcon collected *in situ* data at four levels between the altitudes of 6 and 12 km in a section from Munich to Vicenza (Italy) together with in-flight measurements from smaller aircraft in the lower northern half of the section (Hoinka 1985). Mesoscale wave structures were inferred by manual isentropic analyses in this section and turbulence reports. The focus of the study was to estimate the vertical flux of horizontal momentum. This was later compared with a fully three-dimensional nested simulation with mesh size down to 2.5 km and initialized with a single upstream sounding objectively derived from data from the European radiosonde network (Hoinka and Clark 1991). A synthesis of the few föhn events probed by aircraft outside of a co-ordinated campaign until 1987 is given by Hoinka (1990).

During the preparation phase of the MAP SOP, experiences from campaign-oriented real-time forecasts of stratospheric mountain-wave events over Scandinavia (Dörnbrack *et al.* 1998) were applied to the Alpine region. Schmid and Dörnbrack

(1999) investigate the 7–13 January 1996 south föhn episode with a nested simulation down to a 6 km grid. Above the eastern Alps updraughts of 3 m s^{-1} at 8 km altitude are calculated to be collocated with a strongly decelerated jet and possible wave breaking indicated by steep isentropes and areas of reduced Richardson number. The comparison with observations, radiosoundings in Innsbruck and Munich, as well as turbulence reports from commercial airliners backs the simulations, but remains necessarily fragmentary.

As the entire gravity-wave part of MAP (project P6), the observations of this case-study revisit the investigative path already trodden in Germany and France between 1937 and 1959, but with the technical means of today. Sailplanes flown by sportive scientists are replaced by the jet-propelled research aircraft Falcon of the Deutsches Zentrum für Luft- und Raumfahrt (DLR) cruising at heights between 11 and 12 km*. Pressure and temperature recordings are augmented by sophisticated sensors to determine wind velocity in all three components. A downward-looking laser system operating at a sampling frequency of 100 Hz yields insights into the over-flown cloud decks and pinpoints, when the clouds are not too thick, the mountain ridges below. Three sondes dropped during one of the six repetitive flight legs partially reveal the fine-scale structure of the high-level jet and anomalies in potential temperature. Photographs from the cockpit show the cloud structures as an observer could see them. Images from the National Oceanic and Atmospheric Administration (NOAA) and Meteosat satellites are used to infer wave-induced cloud bands off the aircraft track. The larger-scale atmospheric state is inferred from current analyses by the European Centre for Medium-Range Weather Forecasts (ECMWF). The measured evidence is checked against an episode simulation obtained from the up-to-date non-hydrostatic modelling system Meso-NH. As the brief literature review made clear, such three-dimensional simulations at high resolution, containing moist processes and driven by large-scale fields evolving with time only became feasible very recently.

3. Aircraft equipment and modelling systems

The research aircraft Falcon of DLR, a modified twin-engine business jet with about a 12.5 km service ceiling, served as the only airborne measuring platform during the gravity-wave mission of 25 October 1999. Standard flight-level temperature data are analysed at a rate of 1 Hz using Rosemount PT500 and PT100 sondes for temperature (absolute accuracy ~0.5 K; relative accuracy ~0.1 K). Airflow relative to the plane is determined using a five-hole probe mounted on a 1.8 m nose boom, the aircraft velocity relative to the earth is measured via an inertial navigation system and GPS sensors, and the three-dimensional wind velocity is determined as the difference between the former two large vector quantities. Sources of errors in the wind processing include strong atmospheric turbulence and slow (>1 h) systematic drifts in the navigation system; along straight flight segments on constant pressure levels conservative estimates amount to 1.5/0.3 m s^{-1} and 0.3/0.05 m s^{-1} for the absolute/relative accuracies of the horizontal and vertical wind components, respectively (details in Bögel and Baumann 1991; Quante *et al.* 1996).

Dropping sondes on small parachutes from an aircraft provides a means of obtaining synchronous direct measurements of pressure, temperature, humidity and wind from a dimension other than the aircraft track. Only recently could the sondes and the data link

* It was planned to probe the mid-tropospheric levels with the research aircraft Electra of the National Center for Atmospheric Research. Unfortunately her mission had to be cancelled at the last minute due to a severe temporary health problem of the flight engineer.

TABLE 1. CHARACTERISTICS OF SONDE DROPS ALONG FLIGHT LEG 5

No.	Time (hhmmss UTC)	Latitude (°N)	Longitude (°E)	Start height (km)	Stop height (km)	Fall time (s)	Mean fall speed (m s^{-1})	No. of data points
1	090147	47.58	12.84	12.07	1.66	457	22.8	428
2	090437	47.33	12.76	12.08	2.57	375	25.4	271
3	091232	46.66	12.45	12.07	8.31	268	14.0	755

back to the aircraft be sufficiently miniaturized (total weight less than 500 g) to make drops over land feasible (Hock and Franklin 1999). On 25 October 1999 the first ever drops from the Falcon were undertaken during a field campaign. Three sondes dropped within 11 minutes on one particular flight leg provided useful data as summarized in Table 1.

Downward-directed remote sensing with laser pulses offers a continuous monitoring technique for the vertical plane underneath the aircraft track. The new Differential Absorption Lidar (DIAL) of DLR with high average output power for increased spatial resolution and accuracy was operated on the Falcon for the first time during a campaign. It provides simultaneous measurements of atmospheric backscatter and, in the absence of clouds, water-vapour concentration. Backscatter is sampled at a 100 Hz repetition rate using pulses of the fundamental output wavelength of 1064 nm, of 15 ns duration and with an energy of up to 100 mJ. The backscattered light is collected with a 35 cm Cassegrain-type telescope with 500 cm focal length and an adjustable field of view, typically set to 1 mrad (for details see Ehret *et al.* 2000; Poberaj 2001). The backscatter data are available at a maximum spatial resolution of 20 m (15 m) in the horizontal (vertical) direction, which are here averaged to 200 m and 30 m, respectively.

The large-scale atmospheric state is inferred from ECMWF analyses. The operational horizontal resolution during the MAP SOP was about 60 km (T319) while it was reduced to about 40 km (T511) in November 2000 (Simmons and Hollingsworth 2002). A complete re-analysis of the MAP SOP period applying this increased resolution and including the bulk of the campaign data is underway. We present results from its control run which does not contain all experimental campaign data.

For the mesoscale area of interest, the numerical tool against which to check and interpret the observations is Meso-NH, a three-dimensional, non-hydrostatic research model jointly developed at Laboratoire d'Aérologie and Météo-France. This model is based on the primitive equations in an anelastic formulation. The equations are integrated in a system of curvilinear coordinates with non-uniform grids: geographic conformal projections on a horizontal plane combined with a vertical coordinate based on geometric height and following the prescribed topography. For the spatial discretization, a staggered grid (C-grid) is used. Time integration is achieved by a three-time-level leapfrog scheme with a time filter. In this study we make use of a threefold two-way nesting technique with horizontal mesh sizes of 32, 8 and 2 km. Model orographies are specified from a high-resolution database by averaging over each grid mesh and subsequent filtering over two meshes. Horizontal diffusion is introduced by a fourth-order operator in all prognostic equations to damp the short numerical waves. At the lateral boundaries radiative or open conditions are envoked. The top boundary is a rigid horizontal lid combined with an absorbing layer below to prevent the unrealistic reflection of gravity waves. Here, 50 non-equidistant levels are used in the vertical between the specified terrain and the model top at 20 km (about 50 hPa). More details can be found in Lafore *et al.* (1998) for the model dynamics and numerics and in Stein *et al.* (2000) for the two-way nesting and parametrizations of moist processes. The initial and

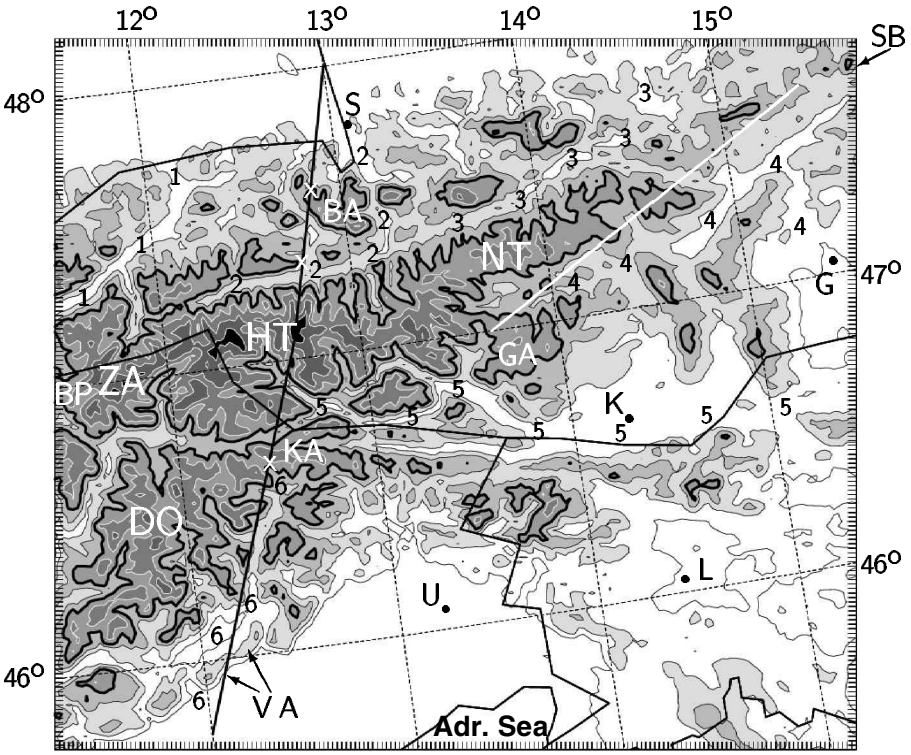

Figure 1. Area of mesoscale interest—eastern Alps between Brenner Pass and Schneeberg. Terrain elevations as resolved with a horizontal resolution of 2 km (innermost simulation domain: height increment 400 m; above 800 m shaded; 1600 m isoline bold; above 2800 m solid black). The tick marks at the circumference indicate the 180 × 160 mesh squares on the stereographic projection plane. Latitudes and longitudes and rough political borders aid the orientation. The black line between 45.75°N, 12.0°E and 48.0°N, 13.0°E indicates the flight track of the Falcon (with a slight bend above the summit of Grossglockner); the white crosses along it mark the positions of drop soundings; the white line marks the baseline of Figs. 10 and 11. Topographic codes: BA = Berchtesgadener Alpen; BP = Brenner Pass; DO = Dolomites; GA = Gurktaler Alpen; HT = Hohe Tauern; KA = Karnian Alps; NT = Niedere Tauern; SB = Schneeberg; VA = Venetian Alps; ZA = Zillertaler Alpen. Towns: G = Graz; K = Klagenfurt; L = Ljubljana; S = Salzburg; U = Udine. River valleys: 1 = Inn; 2 = Salzach; 3 = Enns; 4 = Mur; 5 = Drau; 6 = Piave.

boundary data (for the outermost 4800 km × 4800 km domain) are standard analyses from ECMWF or Météo-France (model ARPEGE). The skill of Meso-NH in simulating Alpine gap flow down to the scale of the Wipptal (between Brenner Pass and Innsbruck) was recently shown by Flamant *et al.* (2002) for MAP IOP 12 on 30 October 1999.

The terrain elevations in the mesoscale area of special interest are given in Fig. 1 as seen by the innermost simulation domain, situated on a stereographic projection plane with 5°E as the perpendicular meridian. The region extends west to east from the Brenner pass to the Schneeberg (not far from Vienna) and south to north from the Adriatic coast to the north-Alpine foreland. The main ridge of the eastern Alps (Ostalpen) consisting in essence of Zillertaler Alpen, Hohe Tauern and Niedere Tauern is completely contained. The shading above 800 m and the bold 1600 m isopleth emphasize the quite realistic structures of the large massifs separated by deep valleys of rivers such as the Inn, Salzach, Enns, Mur, Drau and Piave. Furthermore, the quasi-regular series of side valleys and secondary ridges is evident, which lead to the Salzach and Enns valleys at the northern side of the Hohe and Niedere Tauern massifs. The scale of the map is close to 1:3 million, quite similar to that in any common atlas.

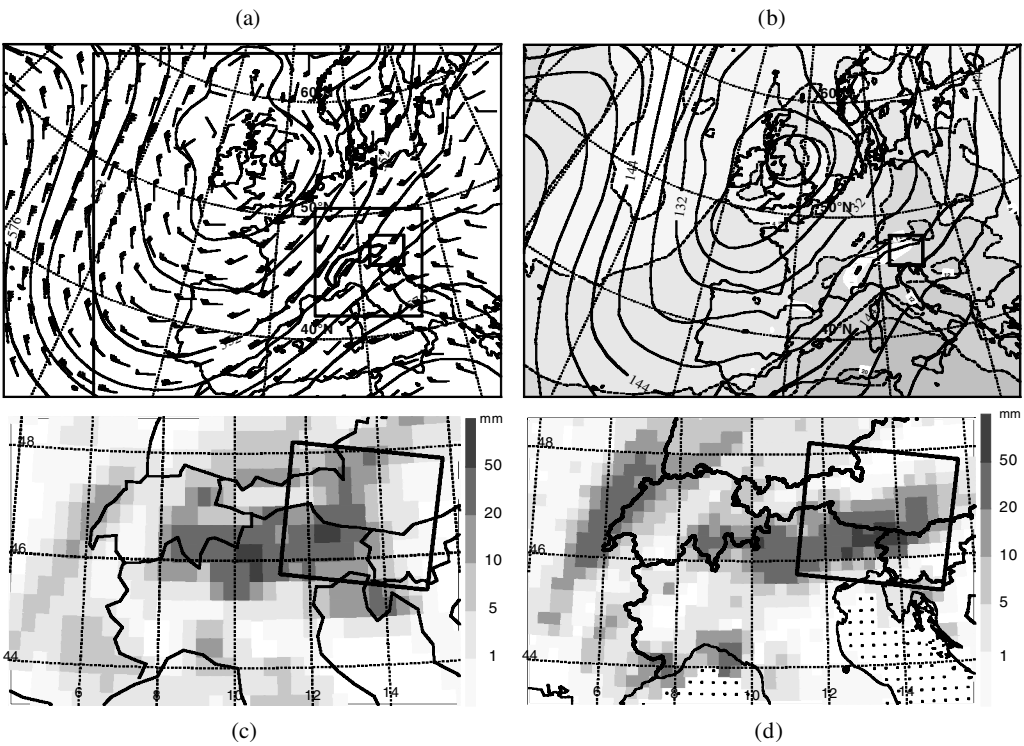

Figure 2. General features of the 25 October 1999 föhn event as diagnosed by the ECMWF re-analysis (T511). (a) Geopotential (gpdam) and horizontal wind (standard barbs in m s^{-1}) at 500 hPa for 00 UTC; (b) geopotential (gpdam) and temperature (white below 0 °C; grey shades with $\Delta T = 4$ K) at 850 hPa for 00 UTC; (c) accumulated 24 h convective plus grid-scale precipitation after 06 UTC. (d) Observed 24 h precipitation after 06 UTC (courtesy C. Frei and MAP Data Centre). The T511 model Alps are indicated by their 1400 m contour in frame (a). The straight lines in frame (a) indicate the borders of the Meso-NH domains, the bold rectangle the innermost one (cf. Fig. 1).

4. OBSERVATIONS

The gravity-wave mission of 25 October was part of IOP 10. *'IOP-10 took place from Sunday to Monday, 24 and 25 October 1999. Events on these days were triggered by an open trough moving eastward from Spain.'* (from the Scientific Director's report*). The general flow, temperature and precipitation patterns are inferred from the ECMWF T511 reference re-analysis which does not yet contain all the campaign data. At 00 UTC on 25 October geopotential and wind vectors at 500 hPa clearly depict the trough spanning more than 20° in latitude and inducing a strong (up to 70 m s^{-1}) south-westerly flow towards the Alps (Fig. 2(a)). Within the large zone of northward-reaching warm air ($T \geqslant 8$ °C) a föhn-induced still warmer patch ($T \geqslant 12$ °C) is apparent in the 850 hPa level north of the Alps (Fig. 2(b)). During 25 October significant precipitation amounts were observed at the windward southern flank of the eastern Alps (maxima exceeding 100 mm 24 h^{-1} near the triple point between Austria, Italy and Slovenia, Fig. 2(d)), as is often the case during föhn events. The sharp gradients and the mostly dry zone to the north of the main Alpine crest in Austria are not reproduced in the global simulation (Fig. 2(c)). All of the following is restricted to our mesoscale area of special interest,

* http://map.ethz.ch/sop-doc/catalog/iop /IOP_10/19991024.MAPSD.txt, September 2002.

obviously quite a small region within the general flow pattern of the Atlantic–European sector.

A pre-MAP modelling study making use of aircraft data from a föhn event in October 1987 indicated that long straight and repetitive flight legs, which are roughly aligned with the ambient wind and run right across the highest ridges, give the best chance of probing well developed mountain waves and possibly their breaking (Doyle *et al.* 2002). Forecast information from the pre-mission days pointed to the eastern Alps and the Hohe Tauern range in particular, as the most promising location. The flight traverse was devised as shown in Fig. 1, with a slight bend above the summit of Grossglockner due to air-traffic control demands. In turn, we now present *in situ* measurements as well as remotely sensed Lidar and dropsonde data gathered onboard the Falcon; this is followed by satellite information from areas away from the aircraft traverses.

(*a*) *Aircraft in situ measurements*

The Falcon entered the first traverse from the north at 0708 UTC (at latitude $\phi = 47.8°$N) and flew over, in a southbound direction, the steep western flank of Hochkalter (2200 m) at the western end of Berchtesgadener Alpen, the valley of the Salzach, the summit of Grossglockner (3797 m) in the Hohe Tauern, the valleys of Isel and Drau, the Karnian Alps, the eastern flanks of the Dolomites along the Piave Valley, the basin of that river, and the range of the Venetian Alps, before passing $\phi = 45.8°$N at 0731 UTC (Figs. 1 and 3). During the following 2 h 11 min this track was repeated five more times before the Falcon had to leave leg 6 at $\phi = 47.3°$N. Legs 1 to 4 were flown at an altitude of 11.4 km (flight level 37 000 ft), legs 5 and 6 at 12.1 km (flight level 39 000 ft).

The sections of vertical velocity (Fig. 3) clearly exhibit wave-type variations of consecutive upward and downward motions up to ± 2 m s^{-1}, a bit more pronounced in the earlier and lower traverses. Over the 140 km distance between latitudes 46.4° and 47.6°N ten peaks and troughs are evident, most regular in legs 1 and 5, yielding $\lambda = 15$ km as an average wavelength along the flight track for vertical velocity. Three regions of quasi-stationary response appear as geographically linked to the eastern Dolomites, the lee of Grossglockner and the Hochkalter further downstream. Across the latter two regions the potential temperature on constant pressure drops by about 5 K on all traverses, thus indicating a consistent wave-generated rise of the isentropes. The three quite evenly spaced drops between latitudes 47.2° and 47.6°N (45 km) indicate 22 km as a wavelength for potential temperature.

(*b*) *Remotely sensed lidar sections*

Detailed cloud backscatter information is available for flight legs 3 to 6 (Fig. 4). On the lee side (north of 47.2°N) consecutive series of ground returns were registered, especially well on leg 3. As verified with a 1:500 000 oro-hydrographic map these precisely depict the succession of mountain flanks and valleys below the flight track north of Grossglockner and to the west of the Zell am See area (from south to north: Salzachtal, Glemmtal, Leoganger Tal, Saalachtal, and Hochkalter with its steep southern flank).

The undulations within the cloud shields, the consistent cloud gap in the lee of the main ridge and the cloud waterfall on its lee slope are taken as relevant gravity-wave indicators. The upstream cloud deck is organized in several strata, because south of the Hohe Tauern ($\phi \leqslant 47.1°$N) return signals from up to three layers could be sampled before the laser's energy was completely absorbed (Fig. 4; letters a, b, c in leg 5). Cloud boundaries and inner cloud zones of high backscatter exhibit distinct vertical variations,

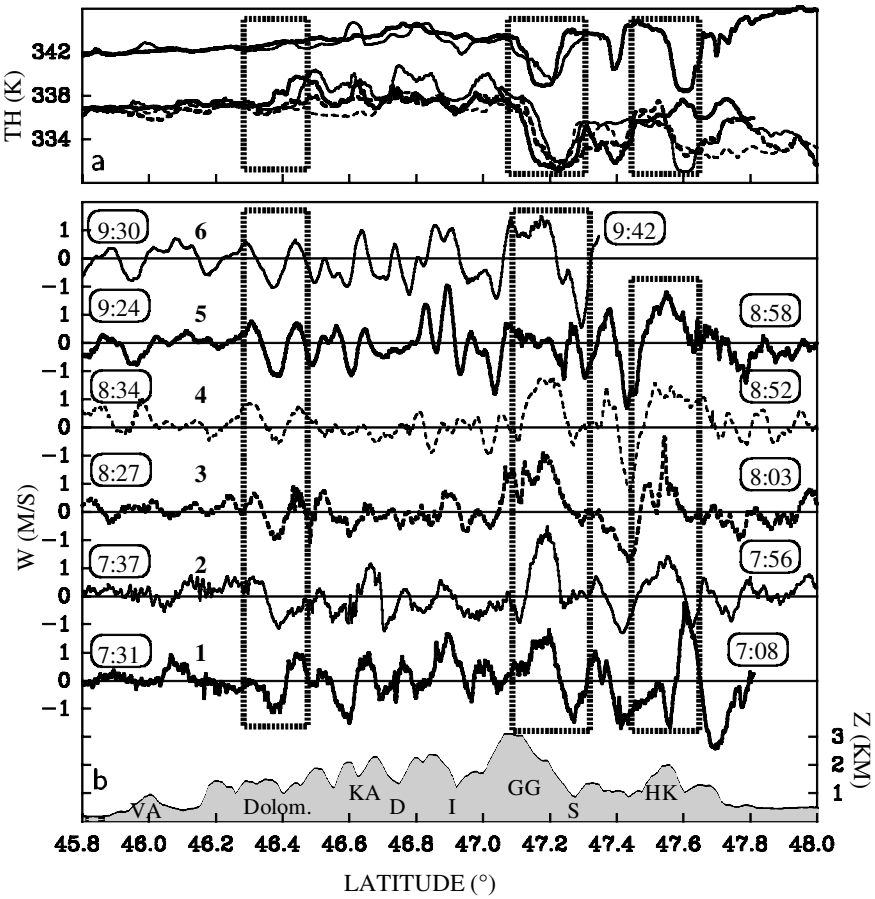

Figure 3. Flight-level data of vertical velocity (W, (b)) and potential temperature (TH, (a)) along six repetitive flight legs executed between 0708 and 0942 UTC on 25 October 1999 (bold lines represent traverses 1, 3, and 5 from north to south, thin lines the return legs 2, 4, and 6). Start and end times of each leg are indicated at the edges (legs 1 and 6 are incomplete to the north). Legs 1 to 4 were at a flight altitude of 11.4 km, legs 5 and 6 at 12.1 km (cf. higher potential temperatures). The underlying orography is extracted from a 2 km resolution dataset (cf. Fig. 1). Topographic codes: VA = Venetian Alps; Dolom. = eastern ranges of the Dolomites; KA = Karnian Alps; GG = Grossglockner (highest summit of Hohe Tauern range); HK = Hochkalter; D = Drau; I = Isel; S = Salzach. The dashed boxes designate regions of quasi-stationary wave response above Dolomites, Grossglockner and Hochkalter, respectively.

although somewhat irregular. Downstream of the gap above the Salzach Valley up to three much more regular undulations are evident in legs 4 to 6 with a mean horizontal extent of about 15 km and a vertical amplitude of about 0.5 km. The gap in the cloud system strongly indicates the systematic wave-induced subsidence in the lee of the main ridge. Striking is the apparent plunging down of the clouds along the lee slopes of the Hohe Tauern range over a depth of at least 2 km. Küttner (1939) termed this feature Wolkenwasserfall (cloud waterfall). It was similarly observed during MAP by the same Lidar system in the lee of Mont Blanc on 2 November 1999 (Smith *et al.* 2002, their Figs. 4 and 5). Possible explanations for the sustained presence of clouds alongside the warming in descending air is discussed below with the simulation results.

The visual appearance of the cloud gap over the sequence of ridges to the north of the main crest and the Salzach Valley, of rugged cloud boundaries to the south and

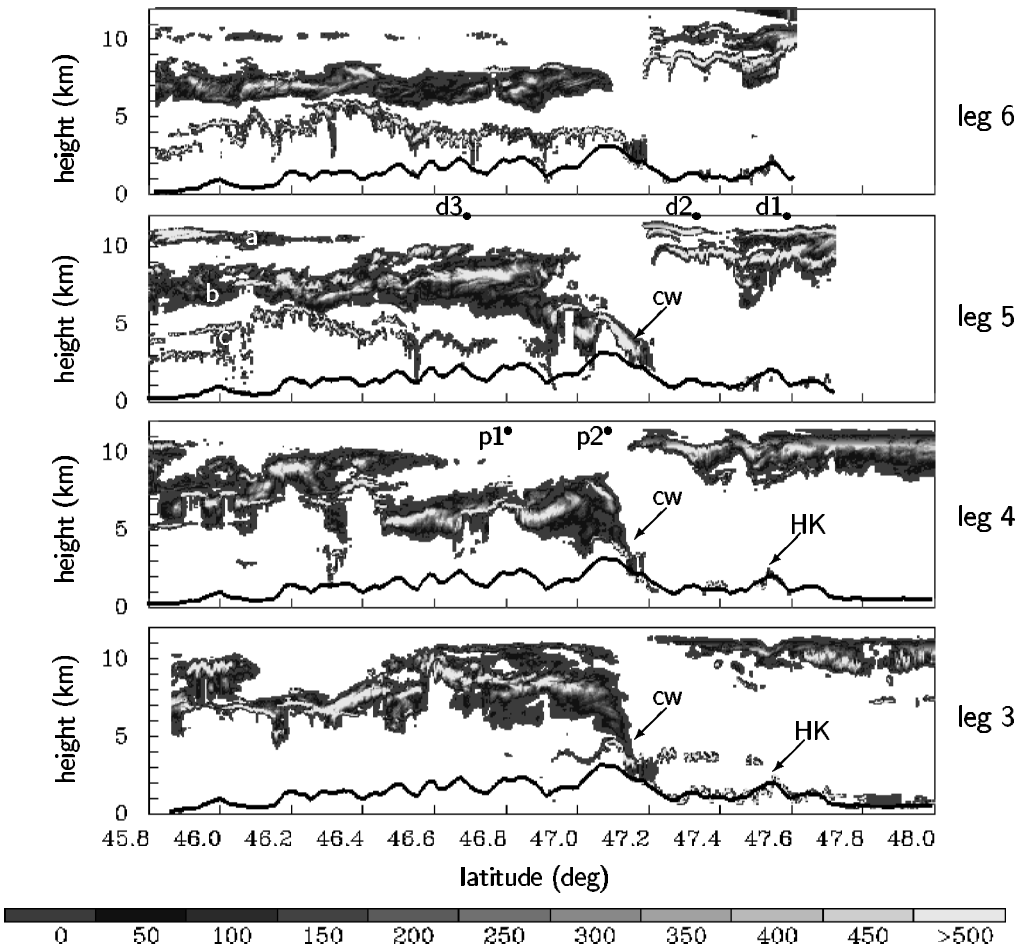

Figure 4. Backscatter ratio of cloud layers, including a cloud waterfall (cw) observed with a downward-looking Differential Absorption Lidar (DIAL) laser system on flight legs 3 to 6 (regions with values below the lidar's detection limit are white). The topographic silhouette is from the 2 km dataset as in Fig. 3 (different aspect ratio); it passes better resolved ground returns north of 47.2°N (especially in leg 3, HK = Hochkalter). Positions p1, p2 = photographs on leg 4 (Fig. 5); d1, d2, d3 = dropsoundings on leg 5 (Fig. 6). Layers a, b, c as indicated near 46.0°N in leg 5.

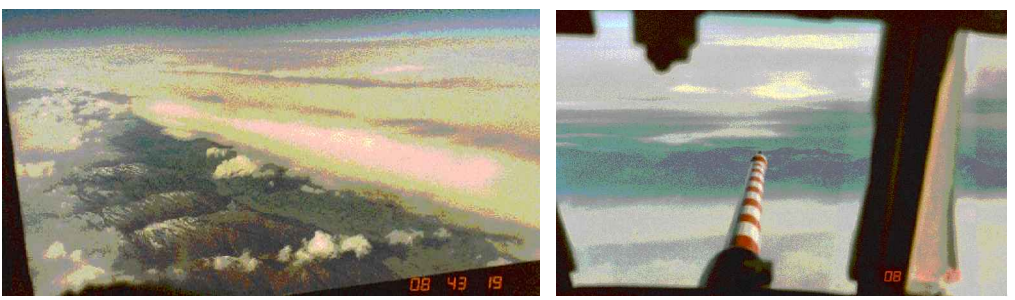

Figure 5. Cloud gap above the Salzach Valley seen from the Falcon cockpit on leg 4. Northward view, looking straight ahead (p1 at 46.8°N, right) and westward view from the left window into the upper Salzach Valley, north of the snow-covered indented ridges extending from the Hohe Tauern main crest (p2 at 47.1°N, left).

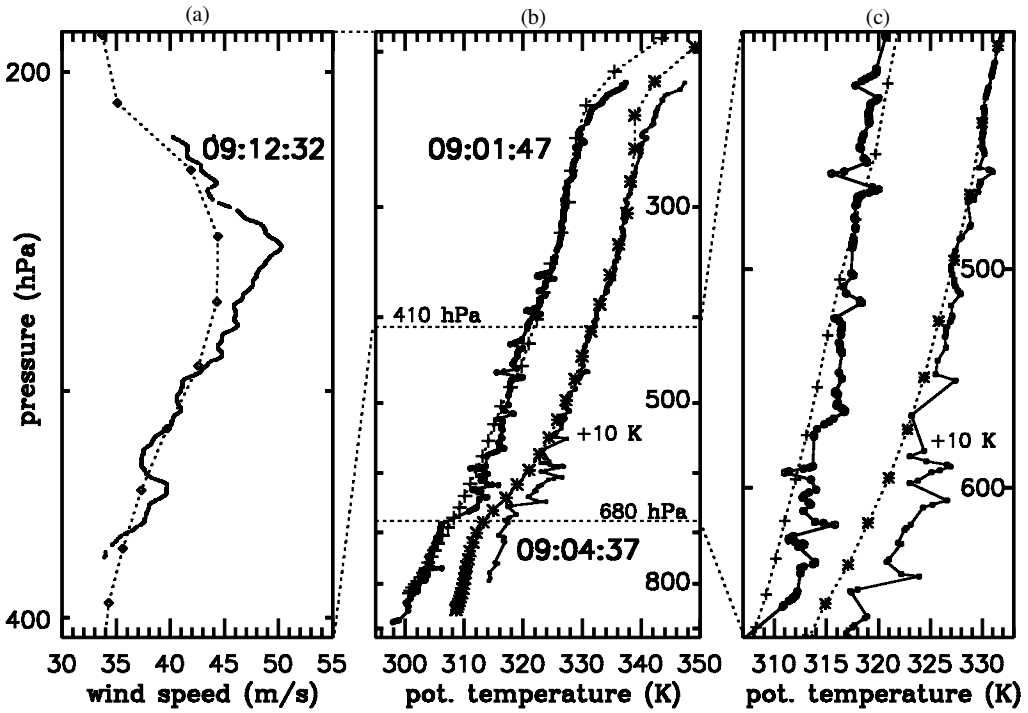

Figure 6. Sonde data from three drops along leg 5 juxtaposed with simulated profiles (dashed, with symbols at model levels). (a) Wind speed in the upper troposphere (0912:32 UTC, sonde d3 in Fig. 4); (b) potential temperature from drops at 0901:47 UTC (open circles, d1 in Fig. 4) and at 0904:37 UTC (filled circles, d2, shifted by 10 K) with complete profiles; and (c) close-up of the mid-tropospheric range with layers of large vertical gradients. Circles denote the individual data points. Tick marks in logarithmic pressure scale every 100 hPa.

the smooth undulated surface to the north were documented by photographs from the Falcon cockpit as well as several lee-side cloud layers (Fig. 5).

(*c*) *Dropsonde information*

Along the southbound flight leg 5 three sondes were dropped within 11 min or separated by 100 km: the first at 0901:47 UTC north of the Hochkalter, the next at 0904:37 UTC to the north of the Salzach Valley and the last one at 0912:32 above the Karnian Alps (see Figs. 1 and 4 for the positions). The datasets are unfortunately only fragmentary, as no winds could be retrieved during the first two fast drops and the data transmission back to the Falcon ceased at 8.3 km or 379 hPa for the third (Fig. 6).

The flight altitude (12.1 km or 197 hPa) was situated in the region of the thermal tropopause as determined by the routine radiosoundings closest in space and time (Udine at 06 and 12 UTC; Innsbruck at 03 and 12 UTC). This is consistent with the profiles of the two dropsondes which transmitted data throughout the entire troposphere, as the steady increase of potential temperature (θ) with height attains higher values only above 230 hPa (Fig. 6(b)). The overall vertical gradient above 600 hPa amounts to 2.7 K km^{-1} (2.9 K km^{-1}) for the first (second) sounding, which is less than, yet not too far from, the standard atmosphere value for midlatitudes in autumn (4.0 K km^{-1}). Above 320 hPa, however, the stability expressed by the vertical gradient of potential temperature is reduced to 1.6 K km^{-1} for well over a kilometre.

Below a certain pressure level both sondes passed through several shallow layers with strong vertical gradients in temperature and, thus, also in potential temperature (360 hPa for the first sonde, 460 hPa for the second). These anomalies are mostly well sampled, although the data collection was not at regular intervals during the fall (Fig. 6(c)). On the first sounding for example, the 500 m deep layer between 480 and 450 hPa, is sampled by 21 data points with an overall gradient in potential temperature of 1.2 K km^{-1}, i.e. much closer to a neutrally stable stratification compared with the global value given above. This layer contains an anomaly over 250 m, sampled by ten points with a succession of much larger gradients and a change in sign: +40 K km^{-1} (over 50 m); −45 K km^{-1} (over 100 m); 30 K km^{-1} (over 100 m). On the second sounding, situated closer to the main crest, these anomalies are confined to levels below 550 hPa. A certain value of potential temperature (e.g. 315 K) is attained six times at different heights, indicating that turbulent processes and possibly wave breaking create small 'bubbles' of lower and higher potential temperature. Below 680 hPa potential temperature again increases linearly with height, but is shifted towards lower values by 5 to 6 K compared with the upper troposphere. For both soundings the profile of relative humidity (not displayed) exhibits a layer with values larger than 70% between 7 and 10 km, above a dry layer with values below 50% between 4 and 6 km, which is consistent with the absence of cloud in the lidar observation (Fig. 4) and the simulation (see section 5).

The third sounding contains a high-resolution profile, yet only within the layer of reduced stability below the tropopause ($\Delta\theta/\Delta z = 1.7$ K km^{-1}). It is collocated with a strong upper-tropospheric jet attaining a maximum speed of 50.3 m s^{-1} at 250 hPa or 11.2 km (Fig. 6(a)). The wind direction is very uniform and from the south-west, varying between 225 and 240°.

(*d*) *Satellite data*

Satellite data are available during the MAP SOP from two sources: the Advanced Very High Resolution Radiometer (AVHRR) instrument on the NOAA polar-orbiting satellites with a few overpasses per day at 1 km pixel size, and the 5 min rapid scans of the Meteosat-6 stand-by satellite (3 km pixels; Bougeault *et al.* 2001, p. 439). Of the former, a multi-channel Alpine overview in stereographic projection is available for 0728 UTC at the MAP Data Centre*. It shows a frontal cloud band over the western Alps collocated with the leading edge of the synoptic-scale trough (Figs. 2(a) and (b)), thick clouds jammed onto the Alpine crest from the south and quite regular patterns of cloud streets in the eastern part of its lee. Data from both sources are used for comparisons with simulated fields in the next section.

5. Comparisons with simulation

Measurements obtained during field campaigns are necessarily only small and isolated samples from the four-dimensional space–time continuum of the atmosphere, no matter how limited the period and region of the special interest are. The quite recent capability of three-dimensional, nested numerical models to simulate a measurement episode in high resolution from large-scale analyses offers a very valuable tool for putting the collected data into perspective. This allows one to collect independent evidence for the quality of both the data and the model as pieces of a true cross-validation process (Hollingsworth 1994, p. 230). The simulation data presented in

* http://map.ethz.ch/sop-doc/catalog/iop /IOP_10/19991025.FALCON_sat-0728.jpg, September 2002.

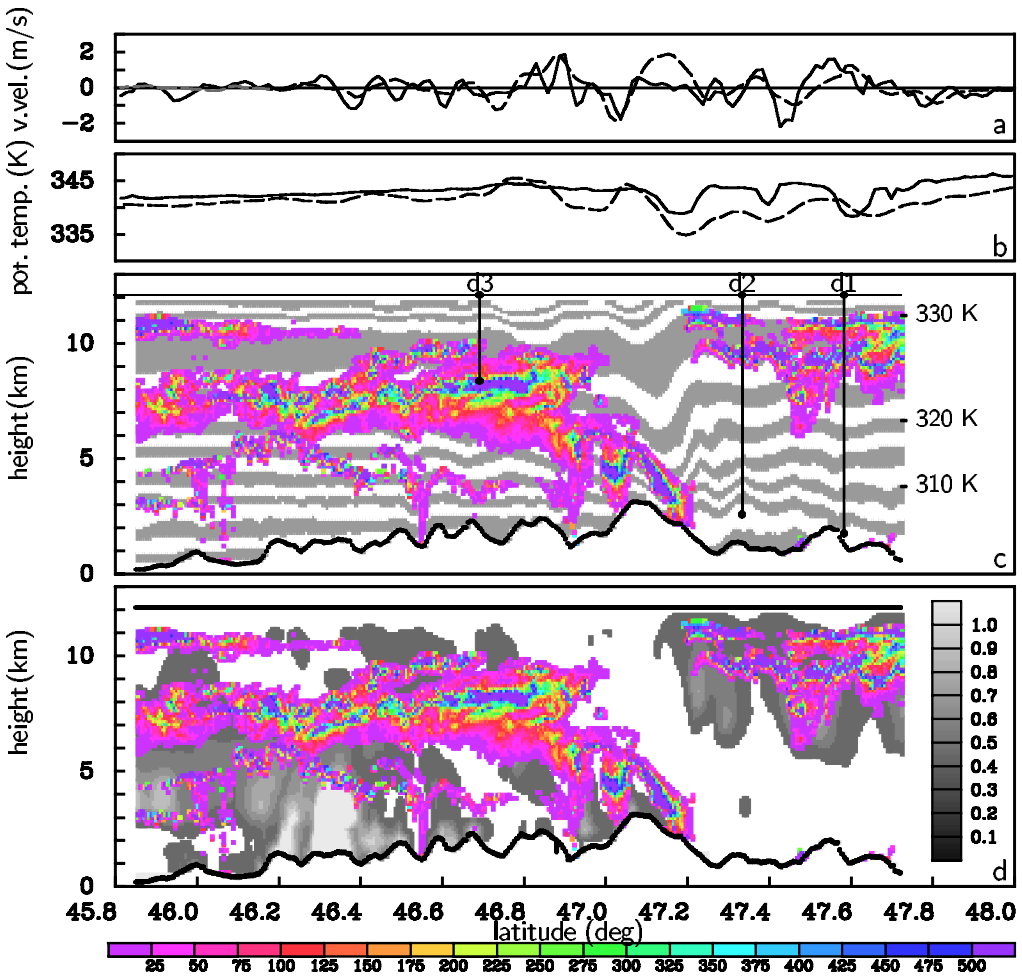

Figure 7. Juxtaposition of various measurements and the simulation along leg 5. (a) Falcon *in situ* vertical velocity; full line measured; dashed line simulated; (b) *in situ* potential temperature; (c) lidar backscatter (in colour) and wave field in terms of simulated potential temperatures ($\Delta\theta = 2.5$ K) below the aircraft track (solid line in 12.1 km) and above the model orography; (d) lidar backscatter and simulated liquid-plus-solid water mixing ratio (g kg^{-1}, values below 0.01 g kg^{-1} left white). The vertical bars d1, d2, d3 in frame (c) designate position and depth of the dropsondes (Fig. 6).

this section stem from the Meso-NH modelling system described in section 3. The simulation was initialized from ECMWF standard analyses (T319 resolution) at 00 UTC on 25 October 1999.

(*a*) *Aircraft section in the model*

The dynamical quantities potential temperature (θ) and vertical velocity (w) along and underneath flight leg 5 are compared in Fig. 7, as they were measured and simulated for 09 UTC together with the cloud structures as seen by the lidar. Along the aircraft path the simulation recovers the range of values and the gross structures of variation in θ and w (e.g. $-2 \leqslant w \leqslant 2$ m s^{-1}) especially downstream of the Hohe Tauern, while the detailed undulations with an average wavelength of about 15 km are not sufficiently

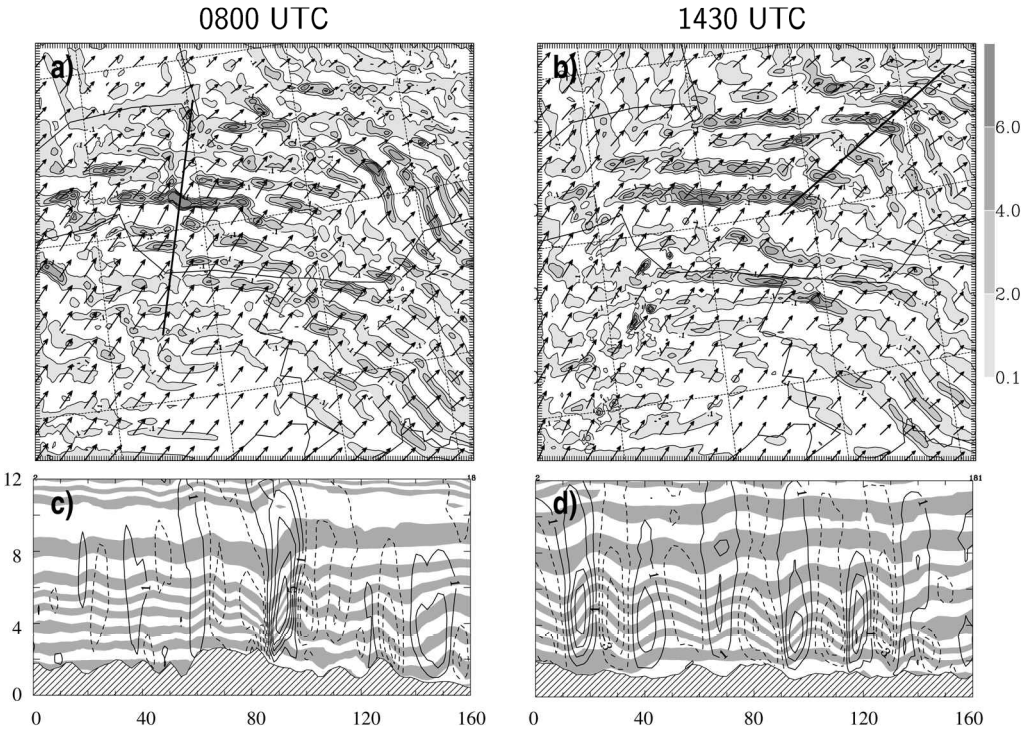

Figure 8. Components of atmospheric flow in particular sections as simulated by Meso-NH. Bands of positive vertical velocity (threshold 0.1 m s^{-1}; Δw = 2 m s^{-1}) with horizontal wind vectors (average speed 25 m s^{-1}) at 5 km for (a) 0800 UTC and (b) 1430 UTC. Cross-sections of vertical velocity (threshold 1 m s^{-1}; Δw = 2 m s^{-1}; negative values dashed) and potential temperature (bands with $\Delta\theta = 2.5$ K) (c) near the Falcon track (0800 UTC) and (d) along the ambient wind through the cloud streets of Fig. 9 (1430 UTC); vertical and horizontal scales in kilometres. Straight lines in (a) and (b) designate the positions of the respective cross-sections.

recovered at the 12 km altitude. Upstream of Grossglockner the potential-temperature trace of the 30 min later-observed leg 6 (cf. Fig. 3) varies more like the simulated one.

Much more illustrative is the complete vertical extent of the simulated wave field as depicted by the stacked potential-temperature bands of $\Delta\theta = 2.5$ K collocated with the lidar view of the cloud structures (Fig. 7(c)). Moderate mid-tropospheric waves from the Karnian Alps towards the main crest are followed by a large-amplitude wave ($\Delta z \approx 2$ km) extending through the entire troposphere. Around $\phi = 46.6°$N undulations of the band between the limits $\theta = 317.5$ K and $\theta = 310$ K coincide nicely with the fragmentary cloud boundaries below the thick, somewhat distorted cloud layer centred at a height of 8 km. The cloud waterfall is clearly situated on the descending (upstream) side of the large wave. It has to be kept in mind, however, that direct subsidence from 5 km down to 2 km with a decrease of potential temperature by 15 K would certainly dissipate the sloping cloud layer due to significant warming. Inspection of horizontal flow and moisture charts at crest level and below (not displayed) indicates that moisture is continuously advected along the Salzach Valley from the west.

Downstream of the large wave the undulated upper cloud boundary closely follows the $\theta = 330$ K threshold. Well captured is the approximately 2 km thick layer of reduced stability just below, as it was measured by the dropsondes. In Fig. 6 these profiles are compared with the (strictly vertical) model profiles consisting of 36 levels below 190 hPa. Pressure is used as the ordinate in order to avoid inconsistencies in the

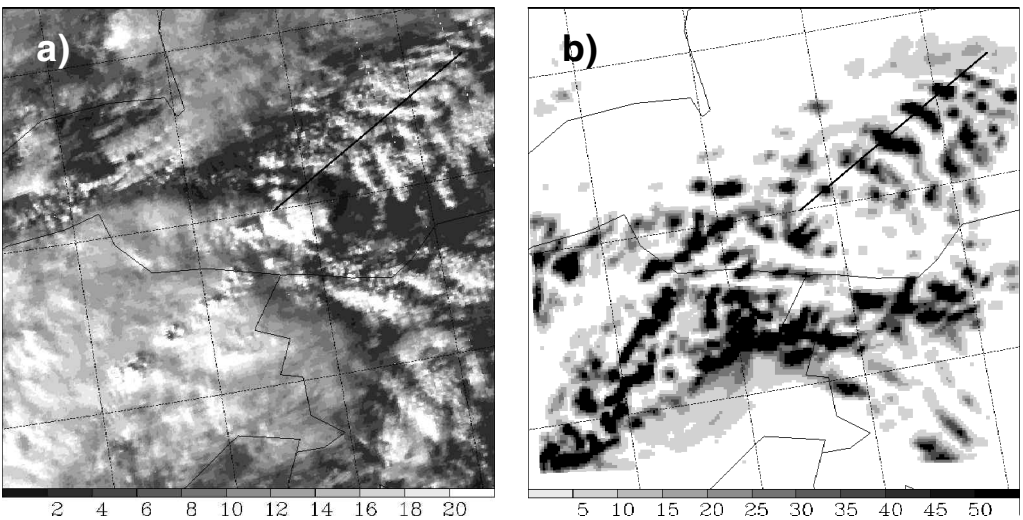

Figure 9. (a) Region of innermost simulation domain as seen by the visible channel of the Advanced Very High Resolution Radiometer (AVHRR) on the National Oceanic and Atmospheric Administration satellite (NOAA-14) at 1422 UTC (radiances in $W\,m^{-2}sr^{-1}$). (b) Simulated vertically integrated liquid cloud water content at 1430 UTC (10^{-5} m). The black south-west–north-east oriented bold line indicates the baseline of Figs. 8(d), 10 and 11.

height determination between model, sonde and aircraft data. In general, the profiles of potential temperature and wind are accurately simulated, although the sharpness of the jet maximum and shallow layers of temperature anomalies could not be resolved properly. Systematic discrepancies in potential temperature are apparent below 400 hPa, particularly in the 0904 UTC sounding (d2 in Figs. 4 and 7); in this region the collocation between sonde and model positions is weakest (for the fast drops (cf. Table 1) no displacement with the not-measured ambient wind is taken into account). Furthermore, localized turbulent mixing may contribute to the measurement–simulation difference. In any case, the simulation demonstrates that the d2 sounding passed the second updraught in the lee of the main ridge below an altitude of 5 km (Fig. 7(c)).

Figure 7(d) demonstrates to what extent the simulated clouds coincide with the complex setting observed by the lidar (three layers upstream, cloud gap over the Salzach Valley, undulated cirrus shield above a less humid cloud-free zone). First of all, the gap is clearly recovered (also in a control simulation initialized from the ARPEGE global model of Météo-France with different background moisture fields), as is the wave-modulated elevated cloud shield downstream above a layer without clouds. Second, upstream of the main crest a complex cloud layer with embedded dry zones is simulated, but not with the triple layering as evident from the lidar data. The comparative simulation from ARPEGE data shows a better agreement in the low-level clouds upstream, but a not so good one at the cirrus level. This reveals the large sensitivity of the simulated cloud structure to the details of initial moisture distribution. Therefore, more systematic numerical experiments appear necessary with increased vertical resolution and more reliably assimilated upstream moisture fields (after the completion of the MAP re-analysis at ECMWF).

A concise depiction of the overall simulated wave response during the Falcon mission is given for 08 UTC in Fig. 8(a). Updraughts in the lee of the main Alpine ridge exceed 5 m s^{-1} in the layer between summit height and 10 km and even 9 m s^{-1} between 4 and 6 km, close to the aircraft traverse (Fig. 8(c)). The horizontal pattern

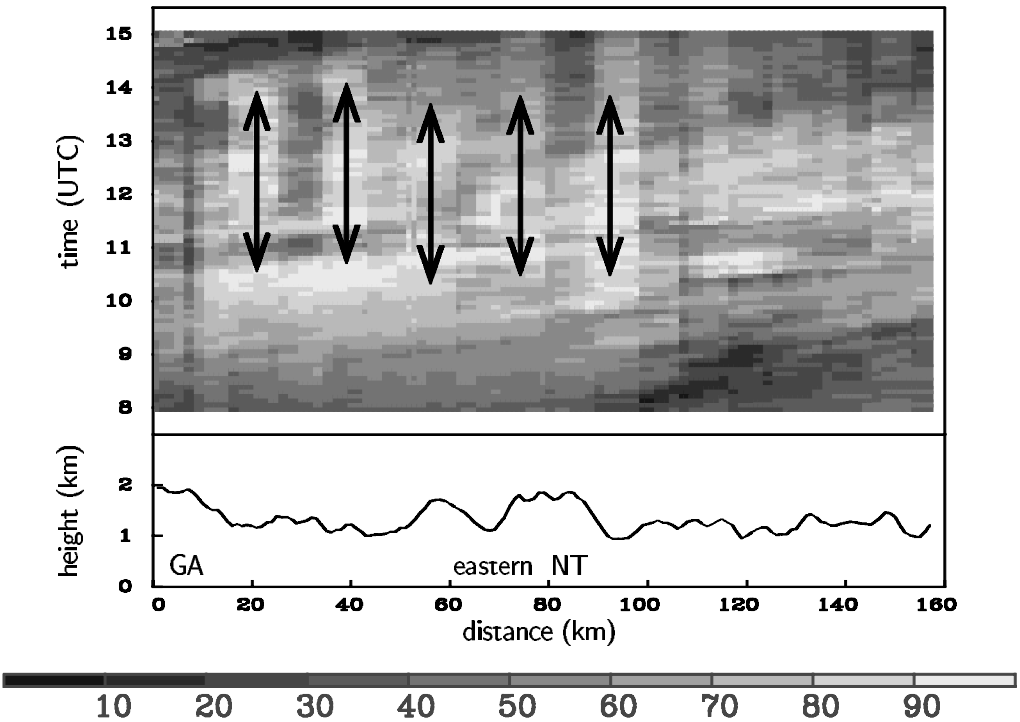

Figure 10. Hovmöller-type time–distance diagram of Meteosat rapid-scan radiances (visible channel in W $m^{-1}sr^{-1}$, top) and Meso-NH model orography (bottom) along the baseline indicated in Fig. 9 from Gurktaler Alpen (GA) across the eastern end of Niedere Tauern (NT, cf. Fig. 1). Vertical arrows show fixed positions of high radiances separated by about 20 km. Effective pixel size of the radiance values: 5 min × 2 km.

of updraughts at the 5 km level consists of a quasi-regular succession of elongated and narrow bands, the orientation of which falls between the normal to the ambient wind and the direction of the main ridges (Fig. 8(a)). The most pronounced zone is the one situated in the lee of the Hohe Tauern and roughly above, yet at some angle to the Salzach Valley. Smaller-scale orographic features apparently modulate the overall pattern to a considerable degree. Further to the east (beyond 14°E) the orientation of the updraught zones is more meridional, parallel to the ranges north-east of Klagenfurt (cf. Fig. 1).

Some six hours later in the simulation the numbers and positions of the updraught bands remain more or less unchanged, but their internal structure appears more consolidated and regular (Fig. 8(b)). Particularly striking is the succession of six waves along the ambient wind in the region where the bands change their orientation (Fig. 8(d)). The cross-section of potential temperature resembles more an environment favourable for the formation of trapped waves (up to 8 km) underneath a layer of slightly reduced, but rather constant stability. Is there any observational evidence for the simulation?

(*b*) *Satellite data and simulated fields*

AVHRR radiances of the NOAA-14 satellite noon overpass at 1422 UTC show quite diverse cloud structures. Figure 9(a) contains the portion which coincides with our region of special interest, displayed in the same projection as in Figs. 1 and 8. Its south-western portion is quite uniformly covered by a cloud deck attaining a mean infrared brightness temperature of 230 K (reflecting about 15 W $m^{-2}sr^{-1}$ in the visible range), apparently the cirrus shield above the precipitating upstream cloud mass. Outstanding is

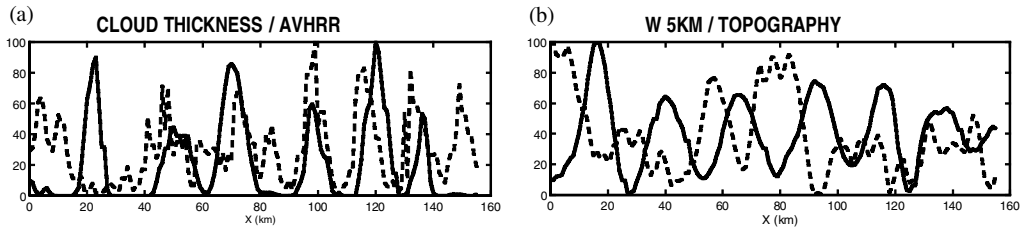

Figure 11. Wave-type variations along the baseline in Fig. 9. (a) Simulated cloud thickness (full line) versus measured Advanced Very High Resolution Radiometer (AHVRR) radiances (dashed line), and (b) simulated vertical velocity (w) at 5 km (full line) versus model topography (dashed line). All values are scaled to a maximum of 100 in order to aid the comparison.

the sequence of six major wedge-shaped cloud lines east of 14°E and north of 47°N. It invokes the common association of lenticularis clouds situated within the crests of lee waves. For these mid-level clouds the most directly related simulated field is the vertically integrated *liquid* cloud water content (Fig. 9(b)) as a measure of their thickness; six bands are simulated for 1430 UTC with shape and position quite similar to the cloud lines in the satellite image.

Visible radiances from the Meteosat-6 rapid scans at 5 min intervals are used to check the stationarity of these cloud bands. A Hovmöller-type time–distance diagram is constructed from all radiance values during the daylight period 08 to 15 UTC and along the baseline as indicated in Figs. 8(d) and 9. Combined with the underlying model topography (cf. Fig. 1) this gives convincing evidence for at least five regularly spaced, bright cloud features which were stationary for some 3 to 4 hours (Fig. 10). Though there are certainly time variations in brightness, the upright stationary features dominate any inclined transients. The variations along the section of the four parameters, AVHRR radiances, simulated integrated cloud water content and vertical velocity at 5 km, as well as the topographic heights, are juxtaposed in Fig. 11. The simulated updraughts are closely related to the topographic profile, yet shifted downstream by about half a wavelength. Model cloud thickness is consistently correlated with the simulated vertical velocity, whereas, AVHRR radiance maxima do not completely coincide.

Four two-dimensional sensitivity experiments were undertaken along this baseline to infer the relative roles of the atmospheric profile and the topographic forcing for the sustenance of the regular waves. According to the classical textbook interpretation these should be solely determined by the background profile and situated downstream of the generating orography. A control run is initialized with a single sounding from the ECMWF analysis at 12 UTC for a location upstream and south of the Alps (46°N, 13°E); it uses the full model orography and is run over 12 h to a quasi-steady state (Fig. 12(a)). A sequence of six regularly spaced updraughts (peak values about 5 m s^{-1}) results as in the section from the fully three-dimensional simulation (Fig. 8(d)). As before, the background stability is reduced in the layer 7 to 10 km, while the lack of smoothing due to lateral adjacent air masses leads to a more noisy response.

Three further simulations use the same set-up, but increasingly longer flat sections at the downstream end of the domain (Figs. 12(b)–(d)). A comparison makes evident that the atmospheric profile alone indeed sustains updraughts spaced by about 20 km, but that the Gurktaler Alpen and the two major ridges in the eastern part of Niedere Tauern (cf. Fig. 10), which happen to be separated by multiples of this distance, significantly enhance the strength of the three eastern updraughts. We conclude that the regular waves

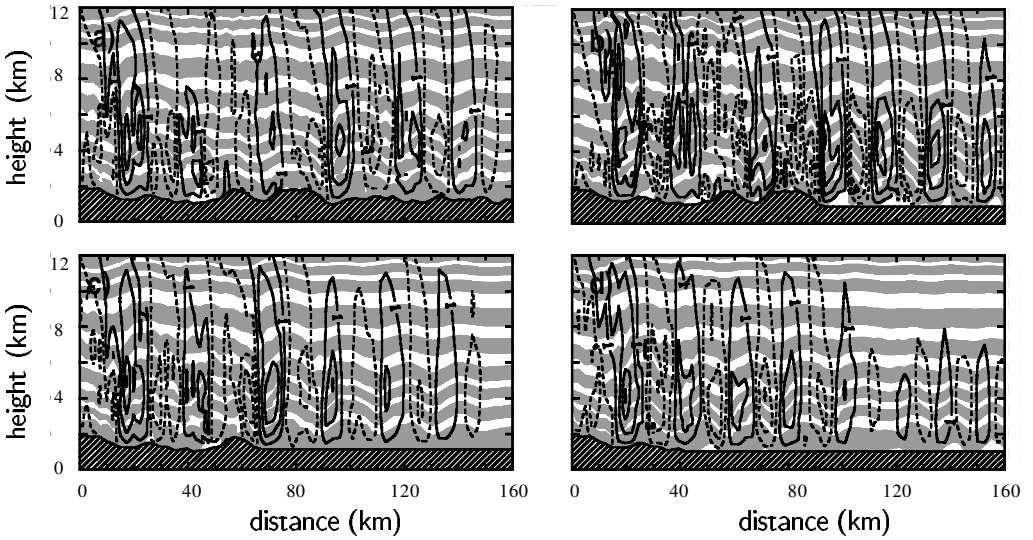

Figure 12. Wave response visualized through potential-temperature layers of $\Delta\theta = 2.5$ K and vertical-velocity cells (full lines upward; increment 2 m s^{-1}) of four two-dimensional sensitivity experiments. (a) Section of Fig. 9 with full orography; (b) to (d) with increasingly longer horizontal planes downstream.

in the full simulation and as evidenced by the satellite image are a synergetic result of the atmospheric profile and repeated forcing by the suitably spaced underlying terrain.

6. Concluding remarks

The literature review (section 2) and the results presented in sections 4 and 5 help to assess the value and novelty of this study. First, various combinations of data types (*in situ* and remotely sensed) and simulation forms (two- and three-dimensional; single-sounding initialization and full transient large-scale forcing) are available for different major mountain ranges and have become more comprehensive during the past years. The possibility of realistically simulating episodes with grid sizes down to a couple of kilometres only evolved during the last decade, just as the availability of dropsonde data over land and detailed laser measurements through cloud layers increased.

Second, although the excited dominant wavelength depends much upon the structure of the underlying terrain, the range of 10 to 25 km appears to be common to most cases. The dominant waves along the aircraft section and detected by the satellite belong to this category (Figs. 3, 9 and 11) and they were found to be essentially stationary over a period of at least two to three hours.

Third, the Alpine topography with differently orientated massifs and ridges separated by deep and long valleys (height variations of more than 2 km over less than 10 km in many places, cf. Fig. 1) induce more irregular wave fields than, say, the Rocky Mountains near Boulder, or the Pyrenees. Yet, the chosen observation strategy with straight, repetitive flight legs across the highest peak of the eastern Alpine crest (Grossglockner) proved to be successful. The intended mid-tropospheric traverses of the Electra would have allowed the verification of the simulated updraughts exceeding 9 m s^{-1} (Fig. 8(c)). The fortunate existence of mid-level cloud bands unshielded by cirrus provided valuable evidence for the wave structures away from the aircraft track (Figs. 9–11). A series of two-dimensional sensitivity experiments indicates that the regular sequence of updraughts, as seen in the satellite image and the simulation, is induced

by the combined effect of the atmospheric background profile and a re-enforcement by the topography below.

Finally, the value of single case-studies is necessarily limited. The unprecedented concerted effort to probe gravity waves during the MAP SOP, however, is also about to provide detailed looks at other wave events; analysed so far are the Hohe Tauern case of 20 September 1999 (Doyle and Smith 2003) and the Mont Blanc case of 2 November 1999 (Smith *et al.* 2002). Climatologically, this sample is being enlarged by systematic evaluations of Global Positioning System data collected during long-range (longer than 1000 km) glider flights back and forth from Vienna to Innsbruck in wave situations. Forstner (2001) presents impressive maps of elongated updraught zones for six events during the years 1997–99 much resembling the simulation result (Fig. 8).

What are the achievements of our synopsis of the 25 October 1999 gravity-wave event over the eastern Alps? A comprehensive combination of aircraft *in situ* data, first dropsonde measurements, detailed backscatter lidar returns from different cloud decks, aerial photography, radiances from orbiting and geostationary satellites with a high-resolution, full-physics episode simulation over 15 h results in an unprecedented detailed view of the atmospheric wave response to the general cross-Alpine flow as it evolved on that day. The episode simulation appears to be a very suitable tool for putting the various observations into perspective. Regional differences (e.g. between the aircraft and satellite sections) are found to be distinctive, whereas the waves within these sections are stationary within 2–3 h. More and complete dropsonde profiles are desirable.

Our approach was a phenomenological one concentrating on the available data. Follow-on investigations are deemed necessary regarding systematic numerical experiments. They should address *inter alia* the sensitivity of the simulated waves to the model resolution in the vertical, to details of the upstream moisture field, and to consolidated large-scale fields (when ECMWF has completed the T511 re-analysis of the entire MAP SOP). Altogether, gravity waves over terrain as complex as the Alps continue to be a difficult and demanding topic of the atmospheric sciences. For instance, other observations during the MAP SOP indicate that mountain waves are instrumental in the formation of cut-off lows when a potential-vorticity streamer crosses the Alps (Hoinka *et al.* 2003).

ACKNOWLEDGEMENTS

Every case sampled during a large campaign profits from considerable assistance by individuals, groups and institutions. We gratefully acknowledge explicitly: Jim Doyle, Ron Smith and Klaus-Peter Hoinka for support during the mission planning; Heinz Finkenzeller and Robert Welser for air-traffic control negotiations and chief piloting; Andreas Giez and Martin Zöger for processing the *in situ* Falcon data; Reinhold Busen for executing and processing the dropsoundings; Andreas Assion and Andreas Fix for their decisive contributions in assembling and operating the DIAL system. Furthermore, we thank Manfred Reinhardt and Paul Pettré for helping to track the early mountain-wave literature; Ulrich Schumann for strongly supporting DLR's large share in the German contribution to MAP; and especially Joachim Kuettner for his flares of inspiration over all the years after he first pleaded for a *South Foehn Project* (later to be called MAP) in Gnadenwald (Tyrol) on 22 June 1990 (Kuettner 1990). The AVHRR data were provided by the NOAA Satellite Active Archive; the Meteosat data carry the label 'Copyright 2001 EUMETSAT'. The Falcon missions during MAP were jointly funded by DLR and the US National Science Foundation. The Centre Nationale de la Recherche Scientifique/Institut National des Sciences de l'Univers and Météo-France

funded the French participation in MAP and the Institut du Développement et des Ressources en Informatique Scientifique provided computer resources under project 95059-CP1. DLR granted support for one co-author (E. Richard) during an extended stay in Oberpfaffenhofen. Comments from two reviewers and Philippe Bougeault helped significantly to sharpen the line of argument.

References

Bögel, W. and Baumann, R. 1991 Test and calibration of the DLR Falcon wind measuring system by maneuvers. *J. Atmos. Oceanic Technol.*, **8,** 5–18

Bougeault, P., Binder, P., Buzzi, A., Dirks, R., Houze, R., Kuettner, J., Smith, R. B., Steinacker, R. and Volkert, H. 2001 The MAP Special Observing Period. *Bull. Am. Meteorol. Soc.*, **82,** 433–462

Chan, K. R., Pfister, L., Bui, T. P., Bowen, S. W., Dean-Day, J., Gary, B. L., Fahey, D. W., Kelly, K. K., Webster, C. R. and May, R. D. 1993 A case study of the mountain lee wave of January 6, 1992. *Geophys. Res. Lett.*, **20,** 2551–2555

Cruette, D. 1976 Experimental study of mountain lee-waves by means of satellite photographs and aircraft measurements. *Tellus*, **28,** 499–523

Dean-Day, J., Chan, K. R., Bowen, S. W., Bui, T. P., Gary, B. L. and Mahoney, M. J. 1998 Dynamics of Rocky Mountain lee waves observed during SUCCESS. *Geophys. Res. Lett.*, **25,** 1351–1354

Dörnbrack, A., Leutbecher, M., Volkert, H. and Wirth, M. 1998 Mesoscale forecasts of stratospheric mountain waves. *Meteorol. Appl.*, **5,** 117–126

Doyle, J. D. and Smith, R. B. 2003 Mountain waves over the Hohe Tauern: Influence of upstream diabatic effects. *Q. J. R. Meteorol. Soc.*, **129,** 799–823

Doyle, J. D., Volkert, H., Dörnbrack, A., Hoinka, K. P. and Hogan, T. F. 2002 Aircraft measurements and numerical simulations of mountain waves over the central Alps: A pre-MAP test case. *Q. J. R. Meteorol. Soc.*, **128,** 2175–2184

Durran, D. R. 1990 Mountain waves and downslope winds. Pp. 59–81 in *Atmospheric processes over complex terrain.* Meteorol. Monogr., Vol. 23. Ed. W. Blumen. Am. Meteorol. Soc., Boston, USA

Ehret, G., Klingenberg, H. H., Hefter, U., Assion, A., Fix, A., Poberaj, G., Berger, S., Geiger, S. and Lü, Q. 2000 High peak and average power all-solid-state laser systems for airborne lidar applications. *LaserOpto*, **32,** 29–37

Elkhalfi, A., Georgelin, M. and Richard, E. 1995 Two-dimensional simulations of mountain waves observed during the PYREX Experiment. *Mon. Weather Rev.*, **123,** 2149–2164

Flamant, C., Drobinski, P., Nance, L., Banta, R., Darby, L., Dusek, J., Hardesty, M., Pelon, J. and Richard, E. 2002 Gap flow in an Alpine valley during a shallow south föhn event: Observations, numerical simulations and hydraulic analogue. *Q. J. R. Meteorol. Soc.*, **128,** 1173–1210

Forstner, B. 2001 'Untersuchung von Gebirgswellen durch Auswertung von Segelflug- und Radiosondendaten'. Diploma thesis, University Vienna

Georgelin, M. and Lott, F. 2001 On the transfer of momentum by trapped lee waves: Case of the IOP 3 of PYREX. *J. Atmos. Sci.*, **58,** 3563–3580

Gerbier, N. and Berenger, M. 1961 Experimental studies of lee waves in the French Alps. *Q. J. R. Meteorol. Soc.*, **87,** 13–23

Hock, T. F. and Franklin, J. L. 1999 The NCAR GPS dropwindsonde. *Bull. Am. Meteorol. Soc.*, **80,** 407–420

Hoinka, K. P. 1985 Observation of the airflow over the Alps during a föhn event. *Q. J. R. Meteorol. Soc.*, **111,** 199–224

1990 *Untersuchung der alpinen Gebirgsüberströmung bei Südföhn*. DLR Forschungsbericht 90-30, ISSN 0939-2963 (available from DLR, Bibliothekswesen, Linder Höhe, D-51147 Köln, Germany)

Hoinka, K. P. and Clark, T. L. 1991 Pressure drag and momentum fluxes due to the Alps. I: Comparison between numerical simulations and observations. *Q. J. R. Meteorol. Soc.*, **117,** 495–525

Hoinka, K. P., Richard, E., Poberaj, G., Busen, R., Caccia, J. L., Fix, A. and Mannstein, H. 2003 Analysis of a potential vorticity streamer crossing the Alps during MAP IOP 15 on 6 November 1999. *Q. J. R. Meteorol. Soc.*, this issue

Hollingsworth, A. 1994 Validation and diagnosis of atmospheric models. *Dyn. Atmos. Oceans*, **20,** 227–246

Krug-Pielsticker, U. 1942 Beobachtung der hohen Föhnwelle an den Ostalpen. *Beitr. Phys. fr. Atmos.*, **27,** 140–164

Kuettner, J. 1990 'Future activities: South foehn project'. Alpex-regional bulletin, **14,** 5-6 (available from Meteo Swiss, Library, Postfach, CH-8044 Zurich, Switzerland)

Küttner, J. 1939 Moazagotl und Föhnwelle. *Beitr. Phys. fr. Atmos.*, **25,** 79–114

Lafore, J. P., Stein, J., Asencio, N., Bougeault, P., Ducrocq, V., Duron, J., Fisher, C., Héreil, P., Mascart, P., Masson, V., Pinty, J. P., Redelsperger, J. L., Richard, E. and Vila-Guerau de Arellano, J. 1998 The Meso-NH atmospheric simulation system. Part I: Adiabatic formulation and control simulations. *Annales Geophysica*, **16,** 90–109

Leutbecher, M. and Volkert, H. 2000 The propagation of mountain waves into the stratosphere. Quantitative evaluation of three-dimensional simulations. *J. Atmos. Sci.*, **57,** 3090–3108

Poberaj, G. 2001 *Airborne differential absorption lidar for water vapour measurements in the upper troposphere and lower stratosphere in the spectral region around 940 nm*. DLR Forschungsbericht 2000-43, ISSN 1434-8454 (available from DLR, Bibliothekswesen, Linder Höhe, D-51147 Köln, Germany)

Quante, M., Brown, P. R. A., Baumann, R., Guillemet, B. and Hignett, P. 1996 Three-aircraft intercomparison of dynamical and thermodynamical measurements during the Pre-EUCREX campaign. *Beitr. Phys. Atmos.*, **69,** 129–146

Ralph, F. M., Neiman, P. J., Keller, T. L., Levinson, D. and Fedor, L. 1997 Observations, simulations, and analysis of nonstationary trapped lee waves. *J. Atmos. Sci.*, **54,** 1308–1333

Reinhardt, M. 1963 Einige Flugbeobachtungen zu den örtlichen Strömungsverhältnissen bei Südföhn im Raum Innsbruck. *Geofisica e Meteorologia*, **XI,** 1–10

Schmid, H. and Dörnbrack, A. 1999 Simulation of breaking gravity waves during the south foehn of January 7–13, 1996. *Beitr. Phys. Atmos.*, **72,** 287–301

Shutts, G. and Broad, A. 1993 A case-study of lee waves over the Lake District in northern England. *Q. J. R. Meteorol. Soc.*, **119,** 377–408

Simmons, A. J. and Hollingsworth, A. 2002 Some aspect of the improvement of skill in numerical weather prediction. *Q. J. R. Meteorol. Soc.*, **128,** 647–678

Smith, R. B., Skubis, S., Doyle, J. D., Broad, A. S., Kiemle, C. and Volkert, H. 2002 Mountain waves over Mt. Blanc: Influence of a stagnant boundary layer. *J. Atmos. Sci.*, **59,** 2073–2092

Stein, J., Richard, E., Lafore, J. P., Pinty, J. P., Asencio, N. and Cosma, S. 2000 High-resolution non-hydrostatic simulations of flash-flood episodes with grid-nesting and ice-phase parameterization. *Meteorol. Atmos. Phys.*, **72,** 203–221

Volkert, H. 1985 Kelvin-Helmholtz waves above the Inn basin—a snapshot from Spacelab. *Beitr. Phys. Atmos.*, **58,** 136–142

Whelan, R. F. 2000 *Exploring the monster—mountain lee waves: The aerial elevator*. Wind Canyon Books, Niceville, Florida, USA